Ultrasonics 155 (2025) 107694

Contents lists available at ScienceDirect

Ultrasonics

journal homepage: www.elsevier.com/locate/ultras

Estimating the properties of bone phantom cylinders through the inversion of axially transmitted low-frequency ultrasonic guided waves

Aubin Chaboty [a,*], Vu-Hieu Nguyen [b], Guillaume Haiat [c], Pierre Bélanger [a]

[a] PULETS, École de Technologie Supérieure, Montréal, H3C 1K3, Québec, Canada
[b] MSME, CNRS, UMR 8208, Université Paris Est Créteil, Université Gustave Eiffel, F-94010 Créteil, France
[c] MSME, CNRS, UMR 8208, F-94010 Créteil, France

ARTICLE INFO

Keywords:
Axial transmission
Low-frequency ultrasonic guided waves
Cortical bone
SAIGA method
Inversion algorithm

ABSTRACT

Early detection of osteoporosis has increasingly focused on ultrasonic methods, particularly guided waves in axial transmission to assess cortical bone properties. This study demonstrates the potential of low-frequency measurements (<500 kHz) for accurately inferring cortical mechanical and geometrical properties. A custom ultrasonic transducer centered at 350 kHz was used to acquire data, processed via a 2D fast Fourier transform to obtain dispersion curves. These were compared with simulations generated using the semi-analytical isogeometric analysis (SAIGA) method, modeling a quasi-cylindrical bone geometry in void or immersed in olive oil. By incorporating an excitability parameter into the inversion algorithm, the proposed method achieved a less than 5% discrepancy between bone phantom properties determined via SAIGA inversion and bulk wave pulse-echo measurements, demonstrating its accuracy and potential for in vivo applications. Results also showed that high-wavenumber modes predominantly reflect material properties, whereas low-wavenumber modes below 100 kHz are sensitive to the overall bone geometry, highlighting the importance of low frequencies for a global bone characterization.

1. Introduction

Osteoporosis is a bone disease characterized by a reduction in bone strength which increases the risk of fracture [1,2]. Early identification is essential, as it facilitates prompt treatment and fracture prevention. Bone mineral density (BMD) assessment using dual-X-ray absorptiometry (DEXA) has been used as the gold standard for the diagnostics of this pathology. However, BMD alone is not sufficient to assess the risk of fracture [3], and often family history is a more reliable method [4]. A thorough assessment of an individual's bone quality should take into account additional factors, including bone rigidity, cortical thickness, and bone volume fraction [3,5].

Quantitative ultrasound (QUS) techniques have emerged as noninvasive and nonionizing methods in various biomedical applications. This technique is particularly well-suited for evaluating bone quality by measuring ultrasonic wave speed and attenuation [6,7]. Moreover, QUS methods are easy to use and not expensive, which may facilitate the monitoring of the disease.

The use of ultrasonic guided waves is a popular technique employed in nondestructive testing, particularly for analyzing and characterizing materials such as composite or bonded plates [8]. In recent years, this technique has been adapted for examining long cortical bone such as the tibia, radius, and femur [9,10]. Early research on axial propagation mainly concentrated on determining the time-of-flight (TOF) of the earliest detected signal, known as the first-arriving signal (FAS). Subsequently, the speed of the quickest waveform was determined and often linked to the fundamental symmetric mode of a plate [11,12]. Several clinical studies have shown that the FAS velocity can be used to differentiate between healthy individuals and those with osteoporosis [13,14]. Another way to use axial transmission technique is to focus on the dispersive trajectories of the mode propagating in the waveguide. However, these methods involve solving a complex multiparameter problem to access the mechanical and geometrical properties of the bone [15,16]. Inversion algorithms or deep learning analysis can be used in an attempt to match experimental and simulated data. In this context, two approaches can be distinguished: using a simplified model at high frequencies (> 1 MHz), due to high attenuation and limited penetration depth [17], or using a bone representative model at lower frequencies (< 500 kHz), which allows for the estimation of the overall geometry.

At high frequencies, ultrasonic guided waves exhibit a reduced depth of penetration within the medium [17], enabling the approximation of long bone to a plate-like structure. This approximation

* Corresponding author.
E-mail address: aubin.chaboty.1@ens.etsmtl.ca (A. Chaboty).

https://doi.org/10.1016/j.ultras.2025.107694
Received 2 December 2024; Received in revised form 28 March 2025; Accepted 11 May 2025
Available online 20 June 2025

facilitates the analysis and interpretation of wave propagation by treating the cortical layer as a thin plate, reducing the model's complexity. Due to the large number of modes propagating at these frequencies, several parameters of the bone cortex can be retrieved through inversion analysis. Foiret et al. [18] proposed an inverse characterization technique to determine the thickness and bulk wave velocities of *ex vivo* cortical bone samples, utilizing a transversely isotropic free plate model integrated with a parameter-sensitive algorithm. Following this, the same group applied genetic algorithm-based inversion schemes to interpret multimodal datasets, circumventing the need for prior assumptions about mode order [19]. However, the presence of soft tissues in the model adds a significant number of modes and a greater attenuation [20], increasing its complexity when extracting dispersion curves [21,22]. Deep neural networks were introduced as an alternative to inversion algorithms. They overcome the complexity introduced by the bi-layer model, providing better estimates of cortical thickness and properties [23]. While the bone can be approximated as a plate at high frequencies and so simplifying the model, the important number of propagating modes makes the inverse problem a complex endeavor. Additionally, a plate model fails to capture the overall shape of the bone, which is crucial for assessing its structural strength.

Using low frequencies allows the wave to penetrate deeper into the bone cortex, enabling a comprehensive assessment of its entire cross-section. This characteristic makes the use of guided waves at low frequencies particularly useful for diagnosing osteoporosis, which primarily affects the inner part of the structure [24]. However, due to a lower number of modes propagating at low frequencies, less information and bone parameters are likely to be obtained through the axial propagation of guided waves. Previous studies have shown the capability of low-frequency ultrasonic guided waves to estimate the cortical thickness of free isotropic plates, which was later applied to tubular structure and *ex-vivo* bones [25]. Likewise, another research group employed a hollow isotropic cylinder filled with a viscous liquid to assess the thickness of bovine tibia specimens by manually correlating experimental velocities with the phase velocities of simulated modes [26]. Peirera et al. [15] have shown that very low frequencies (under 60 kHz) can accurately retrieve the shape of cadaveric radius specimens by using mode amplitudes in the dispersion curves. Using this principle of amplitude, Chaboty et al. further demonstrated the capability of low-frequency axial transmission technique (under 500 kHz) to precisely measure the thickness and velocities of a bi-layer bone phantom plate with an overlaying soft tissue layer [27]. The dispersive properties of ultrasonic guided wave modes combined with the mode amplitude can compensate for the lack of information encountered when using low-frequencies, providing an accurate estimation of the bone health.

This paper demonstrates the potential of low-frequency ultrasonic guided waves (50–500 kHz) to retrieve the cortical mechanical properties and geometry of a quasi-cylindrical phantom filled with soft tissue. The frequency range enables the determination of velocity parameters and geometrical properties, while the excitability of propagating modes enhances the inversion accuracy. Using the semi-analytical isogeometric analysis (SAIGA) method, a parameterized cortical bone cylinder was simulated to estimate experimental bone phantom properties. Dispersion curves, derived from 2D fast Fourier transform processing of measurements made with a proprietary transducer, were compared with semi-analytical predictions. The inversion algorithm estimated five parameters: longitudinal and shear wave velocities, cortical thickness, mean radius, and density. The manuscript is organized as follows: Section 2 outlines the model, inversion algorithm, and experimental protocols; Section 3 present the sensitivity analysis, dispersion curve fitting, and property estimations; Section 4 interprets the findings, and finally the Conclusion summarizes the study's contributions to ultrasonic guided wave-based bone characterization.

2. Material and methods

2.1. Models and simulations models

A model consisting of a bone phantom cylinder filled with soft tissue, representative of the experimental bone phantom cylinders, was employed for the inversion of experimental dispersion curves. An outer layer of viscous fluid was added to the model to reflect the immersed case. Section 2.1.1 outlines the cylindrical model for the forward simulation in this study. Section 2.1.2 subsequently provides an overview of the SAIGA method for solving the forward problem and details the formulation of the mode excitability employed [28,29].

2.1.1. Numerical model

The model was based on the experimental bone phantom cylinders and assumes a homogeneous, isotropic, cylinder-like structure (Ω^S) of infinite length and constant cross-section of thickness h^S and outer radius r^S along the direction of propagation (e_3). While it does not represent a perfect cylinder to account for the asymmetry of the experimental phantoms, the term "cylinder" will be used throughout the text for the sake of simplicity. This simulated cylinder is filled with soft tissue material (Ω^{fi}). In the second part of the study (Section 3.3.2), this cylinder is then embedded in a viscous fluid (Ω^{fo}) of minimum thickness h^{fo}, square-shaped to reflect the experimental container. Fig. 1 shows a description of the model geometry as well as a photograph of both cylinder phantoms and their cross-section. As it can be seen on Fig. 1(c), phantom cylinders are not perfectly cylindrical with some irregularities in their cross section. Unlike an ideal cylinder, the osteoporotic phantom has a radius ratio ($max(r^S)/min(r^S)$ along the axis of the bone phantom) of 1.106, compared to 1.097 for the healthy bone phantom.

The phantom models only represented the cross-section, with the wave assumed to propagate harmonically along the bone axis (refer to 2.1.2 in the SAIGA method). Consequently, throughout this manuscript, we will refer to this model type as a "2.5D model". In general, 2.5D modeling applies to cases that are two-dimensional in one plane (here, the (e_1) and (e_2) axes) but exhibit some level of variation or complexity in the third dimension (typically the (e_3) axis). This third dimension is often treated in a simplified or approximate way, often by making assumptions regarding its behavior [29,30]. For example, in the context of guided wave propagation in a cylindrical structure, a 2.5D model represents the cross-section of the cylinder in the (e_1-e_2) plane, while the axial direction (e_3) is modeled using an exponential term function of the wavenumber in the wave propagation direction: $\exp[i(k_3 x_3 - \omega t)]$ in Eq. (3). This approach allows capturing the essential physics of the problem while reducing computational complexity compared to a full 3D model.

The cortical layer of the model was defined as homogeneous and viscoelastic with a density (ρ), and longitudinal (c_P) and shear (c_S) wave velocities. Two attenuation coefficients α_P and α_S of longitudinal and shear waves respectively were added to the model for defining the viscoelastic tensor. A ratio α_P/α_S at 1 MHz was fixed at 1.5 [31,32], with $\alpha_P = 2.9$ dB/cm at this frequency, in accordance with the manufacturer properties. The viscosity coefficients were calculated as [20,33]:

$$\begin{cases} \eta_{11} = \dfrac{\alpha_P}{8.686} \times 2c_P \times \dfrac{C_{11}}{(\omega_{ref})^2} \\ \eta_{66} = \dfrac{\alpha_S}{8.686} \times 2c_S \times \dfrac{C_{66}}{(\omega_{ref})^2} \\ \eta_{13} = \eta_{11} - 2 \times \eta_{66} \end{cases} \tag{1}$$

where $\omega_{ref} = 2\pi f_{req}$ with $f_{req} = 1$ MHz the reference frequency used for the calculation of the viscosity tensor. The values of η_{11}, η_{13}, and η_{66} are kept constant within the frequency bandwidth of interest and determined by the value of the attenuation coefficients at frequency f_{req}. The complex elasticity tensor is then expressed as $C^* = C + i\eta\omega_{ref}$.

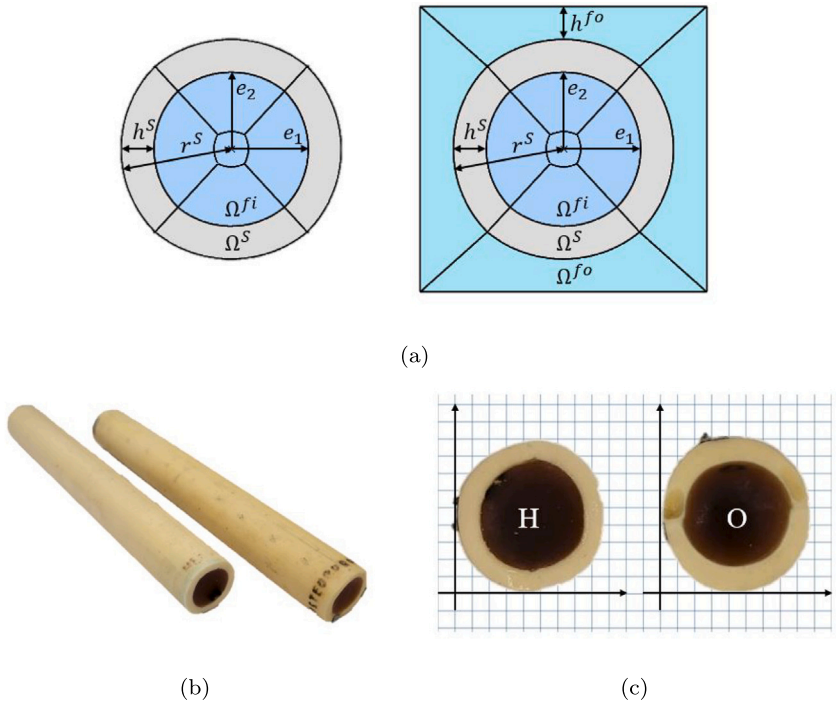

Fig. 1. (a) Geometrical description of the numerical model with and without the outer fluid domain. (b) Experimental bone phantom cylinders measuring 150 mm in length. (c) Cross section of the healthy «H» and osteoporotic «O» bone phantoms.

The inner and outer layers were modeled as linear acoustic fluids of density (ρ^{fi}) and (ρ^{fo}) respectively, with their corresponding wave velocities (c_P^{fi}) and (c_P^{fo}). As the phantoms were provided by the same manufacturer as the plates used in Chaboty et al. [27], the properties of the inner soft tissue were assumed to be the same as the properties of the soft tissue layer used in [27]. Therefore $\rho^{fi} = 977$ kg/m^3 and $c_P^{fi} = 1390$ m/s, with an attenuation coefficient $\alpha^{fi} = 0.6$ dB/cm at 1 MHz. For the outer layer, olive oil was used as viscous fluid for experiments. This choice was made to provide a greater attenuation in comparison with water, while keeping the celerity and the density close to those of soft tissue [34]. As a result, the outer layer's properties were defined with a density of $\rho^{fo} = 913$ kg/m^3, a speed of sound of $c_P^{fo} = 1455$ m/s, and an attenuation of $\alpha^{fo} = 0.05$ dB/cm at 1 MHz [35–37]. The viscoelastic coefficient of both fluids was calculated as follows:

$$\begin{cases} \eta^{f(i,o)} = \dfrac{\alpha^{f(i,o)}}{8.686} \times 2c_P^{f(i,o)} \times \dfrac{K^{f(i,o)}}{(\omega_{ref})^2} \\ K^{f(i,o)} = \rho^{f(i,o)} \left(c_P^{f(i,o)}\right)^2 \end{cases} \tag{2}$$

2.1.2. SAIGA method and excitability formulation

Based on the principles of the semi-analytical finite element method (SAFE) [30,38,39], the SAIGA method is used to compute simulated dispersion curves. The method assumes harmonic wave propagation along the propagation direction (e_3), which corresponds to the cylinder's axial direction. The displacement field $\mathbf{u}$ for the solid layer and pressure field in inner and outer fluids $\mathbf{p}_{i,o}$ can be expressed as:

$$\begin{cases} \mathbf{u}(x_1, x_2, x_3, t) = \mathbf{U}(x_1, x_2) \exp[i(k_3 x_3 - \omega t)] \\ \mathbf{p}_{i,o}(x_1, x_2, x_3, t) = \mathbf{P}_{i,o}(x_1, x_2) \exp[i(k_3 x_3 - \omega t)] \end{cases} \tag{3}$$

where $i^2 = 1$; $\omega \in \mathbb{R}$ is the angular frequency; k_3 is the wavenumber in the direction of propagation (e_3); the vector $\mathbf{U}(x_1, x_2) = (U_1, U_2, U_3)^T$ and $\mathbf{P}_{i,o}(x_1, x_2) = P_{i,o}$ are the amplitudes of the displacement vector in (Ω^S) and of the pressures in ($\Omega^{f(i,o)}$), respectively. The use of the SAIGA method results in a quadratic eigenvalue problem that must be solved to determine the relationship between the wavenumber k_3 and the angular frequency ω. This relationship can be obtained with respect to k_3 as follows:

$$(-\omega^2 \mathbf{M} + \mathbf{K}_0 + ik_3 \mathbf{K}_1 + k_3^2 \mathbf{K}_2)\mathbf{V} = \mathbf{0} \tag{4}$$

where $\mathbf{V} = (\mathbf{P}, \mathbf{U})^T$ denotes the global eigenvector, comprising the pressure eigenvector ($\mathbf{P}$) and the displacement eigenvector ($\mathbf{U}$), while $\mathbf{M}, \mathbf{K}_0, \mathbf{K}_1, \mathbf{K}_2$ represent the global matrices of the system and are not dependent on k_3. The global matrix formulation was detailed by Seyfaddini et al. [28,29]. For every instance of the angular frequency ω, solving Eq. (4) yields the eigenvalues k_3, along with their corresponding eigenvectors denoted as $\mathbf{V}(\omega, k_3)$. These values represent the characteristics of the guided modes. Additionally, the frequency-dependent phase velocity (c_{ph}) and attenuation (att) of a particular guided mode can be calculated using these parameters.

$$c_{ph} = \omega / \Re(k_3)\ m/s \qquad att(\omega) = \Im(k_3)\ Np/m \tag{5}$$

NURBS basis functions of order 3 were used for SAIGA analysis. The model was divided into 4 patches as shown in Fig. 1(a). Every patch was then divided to ensure acceptable precision in the calculation of dispersion curves. Therefore, the number of degrees of freedom for the model accounts for $N_{Dof} = 361$. The dispersion curves were calculated over a frequency range spanning from 50 kHz to 500 kHz, in increments of 5 kHz.

To ensure that the inversion of the experimental dispersion curves was targeting the most significant modes, the excitability Ex for a specific mode was calculated according to its mode shape. Using the same formulation as presented in Chaboty et al. [27] and based on previous works [15,40], the excitability value can be formulated in cylindrical coordinates as:

$$\begin{cases} Ex(k_3, \omega) = \dfrac{\Re(k_3, \omega)}{\Im(k_3, \omega)} \times U_{norm}^2(k_3, \omega) \\ U_{norm}(k_3, \omega) = \dfrac{abs(U_{r,fo})}{max(U_{r,\theta,z})} \end{cases} \tag{6}$$

where U_r, U_θ, U_z are respectively the radial, angular and axial (along (e_3)) displacement through all the layers. $U_{r,fo}$ is the radial displacement at the top surface of the outer fluid. In the case where no outer

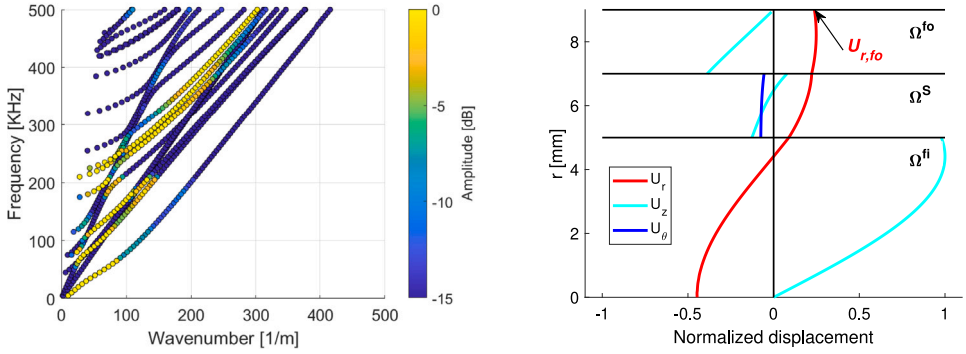

Fig. 2. (a) Guided modes dispersion curves with their frequency-dependent excitability computed by SAIGA for a 3D cortical bone cylinder (ρ = 2310 kg/m^3, c_P = 2900 m/s, c_S = 1600 m/s, h^S = 2 mm, r^S = 7 mm) filled with soft tissue (ρ^{fi} = 1010 kg/m^3, c_P^{fi} = 1400 m/s) and immersed in 2 mm of water. The color scale shows the excitability of each mode in dB normalized to the mode with the highest excitability at each frequency. (b) Mode shape of a selected mode (f = 200 kHz and k = 127 m^{-1}).

fluid is present in the model, $U_{r,fo}$ is replaced by $U_{r,S}$, the radial displacement at the top surface of the solid layer. Fig. 2(a) illustrates an example of the excitability of guided wave modes in a cylindrical model with the presence of the outer fluid layer model as a function of frequency. The color of each circle indicates the amplitude of the mode excitability for each corresponding mode. Meanwhile, Fig. 2(b) presents the mode shapes associated with a selected mode shown in Fig. 2(a), highlighting the various displacements utilized in the calculation of excitability.

2.2. Inversion algorithm

This study hypothesizes that aligning experimental dispersion curves with the simulated ones generated via the SAIGA method can effectively evaluate the properties of the cortical bone layer (c_P, c_S, h^S and r^S). To do so, an inversion algorithm was developed using a cost function as a metric to determine the optimal alignment between the experimental dispersion curves and specific instances within the simulated dataset. It is worth mentioning that the accuracy of the method depends on several factors, including the quality of experimental dispersion curves, the accuracy of the phantom geometry and mechanical properties in the model, and of parameters used for numerical simulations such as the order of the NURBS basis function, grid steps of the simulated dataset and the overall precision of the model.

2.2.1. Formulation of the cost function

By definition, a cost function is a metric to gauge the difference between predicted values from a model, and experimental observations. The minimization of the cost function typically leads to the best fit between the numerical and experimental data. However, the formulation of the cost function may alter the output result and influence the algorithm's performance. Here, dispersive trajectories and excitability of ultrasonics guided waves modes were used and we employed the same cost function as Chaboty et al. used in [27]. The robustness of this function has been successfully validated on a bi-layer plate model. Therefore, the cost function quantifies the difference in magnitude between actual and simulated dispersive curves.

Considering a set of parameters Λ=(ρ, c_P, c_S, h^S, r^S) and Λ=(ρ, c_P, c_S, h^S, r^S, h^{fo}) in the case of the phantom in a free-field and of an immersed phantom respectively, the difference of amplitude for each simulated frequency was calculated as follows:

$$d_n(\Lambda, f) = \left| Ex(k_n(\Lambda), f) - A(k_n, f) \right|, \tag{7}$$

where $Ex(k_n(\Lambda), f)$ represents the simulated excitability of a particular mode at wavenumber k_n and frequency f for a given set of parameter Λ. Similarly, $A(k_n, f)$ is the experimental amplitude observed for the couple (k_n, f).

To prioritize higher-amplitude modes in the inversion process, a weighting factor was introduced. This factor ensured that modes with amplitudes below a user-defined threshold ξ, were discarded from the cost function, while those with the highest amplitudes contributed fully, with a weight of 1. The weighting factor was defined as:

$$\chi_n(\Lambda, f) = \frac{Ex(k_n(\Lambda), f) - \xi}{-\xi} \tag{8}$$

Using these two indicators, $d_n(\Lambda, f)$ and $\chi_n(\Lambda, f)$, the cost function for a particular set of parameters Λ was defined as:

$$J(\Lambda) = \sum_f \sqrt{\sum_{n=1}^{N} (d_n(\Lambda, f).\chi_n(\Lambda, f))^2} \tag{9}$$

where N is the total number of simulated modes for a given frequency. This cost function thus emphasizes high-amplitude modes while disregarding those below the threshold, reducing the risk of incorporating irrelevant information into the inversion. In this study the threshold ξ was fixed at −15 dB. In summary, this cost function calculates the accumulation of errors between the model predictions (for a parameters set (Λ)) and the experimental observations: $d_n(\Lambda, f)$, weighted by $\chi_n(\Lambda, f)$. The objective is to minimize the value of $J(\Lambda)$ by adjusting the set of parameters (Λ).

To ensure compliance with thermodynamic principles and to avoid obtaining results lacking physical meaning or deviating significantly from values reported in the literature [27,41–43], the Poisson's ratio was calculated for each parameter set Λ. Based on reference wave velocity values for the two bone phantoms (see Table 2), the experimental Poisson's ratios for the healthy and osteoporotic cylinders were 0.2365 and 0.2475, respectively. Consequently, a condition was imposed on the Poisson's ratio $\nu(\Lambda)$ for each parameter set. If $0.22 < \nu(\Lambda) < 0.26$, the set was included in the inversion process; otherwise, it was excluded.

2.2.2. Dataset generation

The cost function was calculated for all sets of simulated properties. Each parameter was systematically swept across a multidimensional grid. The range of each parameter was chosen to be large enough to incorporate both properties of the healthy and osteoporotic bone phantom cylinder. Each parameter range was defined large enough to ensure that the measured bone phantom cylinder properties were far enough from the limit values.

Two sets of data were generated. One represented the scenario of free-field bone phantom cylinders, while the other depicted those immersed in olive oil. To reduce computation time, the decision was made to maintain the mechanical properties of both inner and outer fluids constant. The inner portion of the bone phantom cylinder is made

Table 1
Range of model parameters and their respective step used to create the datasets.

	Parameters range	Step
ρ (kg/m^3)	[1900 – 2500]	200
c_P (m/s)	[2450 – 3150]	100
c_S (m/s)	[1400 – 1900]	100
r^S (mm)	[9 – 10.5]	0.5
h^S (mm)	[2.7 – 3.3]	0.2
h^{fo} (mm)	[2.5 – 3.5]	0.5

of soft tissue-mimicking material. Both phantoms were manufactured by the same company that makes the plates in [27]. It was assumed that the properties of the soft tissue mimicking material remain identical. Therefore, $\rho^{fi} = 977$ kg/m^3 and $c_P^{fi} = 1390$ m/s. Properties of the outer fluid correspond to those of olive oil and will remain constant: $\rho^{fo} = 913$ kg/m^3 and $c_P^{fi} = 1455$ m/s. Table 1 depicts the parameters grid.

Parameter steps were chosen by balancing resolution and computational efficiency. Concerning the free-field model, a single simulation took approximately 45 s, whereas in the immersed model, it took nearly 70 s. The server used for calculations was a high-performance GPU-based system, 256 GB of RAM, with dual Xeon Silver 4215 processors (16 cores, 32 threads) which enabled parallelization of the calculus. For both datasets, the total number of cases was 3072 and 9216, respectively. Emphasizing the importance of including all modes, a frequency resolution step size of 5 kHz was chosen, allowing for 90 frequencies to be measured within the 50–500 kHz frequency range. Two comprehensive databases regrouping all the possible cases of both scenarios were created during an extended, continuous modeling session. The free-field database required 36 h to complete, while the immersed database took 180 h (7.5 days) for simulations. Generating datasets for 2.5D models requires a much higher cost compared to 1.5D problems. In our previous study [27], generating 72,600 cases for a 1.5D bi-layer plate model took less than 48 h for computation without using the parallelization.

2.3. Experimental protocols

2.3.1. Bone phantom cylinders and reference values

In this study, two bone phantom cylinders filled with soft tissue-mimicking material were used: one with properties considered as healthy, and the other simulating an osteoporotic state with degraded properties. These cylindrical specimens were made by True Phantom Solutions (Windsor, ON, Canada), are 150 mm long and have a diameter of 20 mm, with a cortical layer thickness of around 3 mm. Additionally, two small blocks representing healthy and osteoporotic cortical layers were provided. Pulse-echo measurements were conducted on these blocks to establish baseline sound velocity values. The sample thicknesses were measured 20 times, followed by an equivalent number of pulse-echo measurements. For these pulse-echo measurements, a longitudinal probe (V125-RM) and a shear probe (V124-RM) from Olympus centered at 2.25 MHz were employed. An Omniscan-X3 from the same company was used to perform the measures. Densities were also calculated based on these samples by weighting them and measuring their volume with a 3D laser scanner (Absolute Arm 85) from Hexagon (Stockholm, Sweden), with uncertainties for each parameter derived from the measurements. To precisely determine the thickness of the cortical phantom layer of each cylinder, 36 measurements were taken across all the phantoms using the longitudinal probe. The baseline velocity values obtained with the block specimens were used to determine the actual thickness of the cortical layer of the cylinders. It was assumed that the cortical layer has nearly-isotropic behavior and was homogeneous. However, the cross-section's geometry of the phantoms were not uniform along their length. In fact, a variation of around 10% was observed in the cortical thickness and diameters. As a result, the mean values will be used for comparison with the inversion results.

2.3.2. Axial transmission setup

A probe was specifically designed and built to perform the ultrasonic excitation. The components have been chosen to provide a central frequency of 350 kHz with −6 dB bandwidth between 150 kHz and 550 kHz. The selected frequency range enables the extraction of the bone mechanical properties as well ass the geometry, making it suitable for a 4 mm thick cylinder. This range can be adjusted based on the target site. Low frequencies are interesting for capturing the full cross-section and retrieving both thickness and radius, while the upper frequency limit can be adapted to obtain the desired number of modes for the inverse process to converge. A combination of specific piezoelectric and matching layer components was used to maximize the transmission of the waves through the bone phantom. Hann windowed tonebursts with a maximum amplitude of 12 V were used to excite the piezoelectric element, with central frequencies varying from 50 kHz to 500 kHz with a step of 50 kHz. The number of cycles was chosen specifically to ensure each toneburst has a bandwidth at −3 dB of ± 50 kHz. The probe has a dimension of 20 × 4 mm with a flat front surface.

For the free-field measurements, where cylinders are not immersed in fluid, the probe was placed in contact with the outer perimeter of the cylinders and coupled with an ultrasonic gel Ultragel® II. A guide ensures the probe is placed normal to the surface with the 20 mm dimension perpendicular to the axis of the cylinders. For the immersed case, a constant outer fluid layer of approximately 3 mm was maintained, with the sensor positioned slightly below the top surface of the fluid. For this, a 3 mm-thick spacer was placed between the cylinder's surface and the probe's face. Positioning is done using the same guide as for the case in air. Once the probe is in place, it is held by a clamp, and the spacer is carefully removed. The probe is therefore positioned 3 mm above the cylinder's surface, perpendicular to the fluid's surface.

Four consecutive acquisitions were realized on the cylinders for both scenarios. After each acquisition, the probe was repositioned and slightly shifted aside for averaging the impact of its position. Acquisitions were carried out along the bone phantom axis at 60 equally spaced positions, 1 mm apart, using a Doppler laser vibrometer (Polytech OFV-505). Two of the four acquisitions were conducted in one direction, with the remaining two measurements performed in the opposite direction, to minimize the effect of possible thickness variations within the fluid layer. In the immersed configuration, the laser was focused on the fluid's surface. The reflective properties of olive oil, attributed to its green hue, facilitated effective signal detection. Conducting the experiments in a darkened environment further enhanced the signal quality.

A TiePie® Handyscope HS3 was used to send the emitting signals to the probe and to acquire the data measured by the laser vibrometer. Experimental data were processed with a 2D fast Fourier transform to obtain experimental dispersion curves [44]. Fig. 3 represents a photograph of the experimental setup along with representative time trace signals recorded in the immersed configuration. These signals represent ultrasonic guided waves measured on the healthy bone phantom immersed in olive oil at points 1, 30, and 60. The waveform evolution during propagation is clearly observed. Despite being the least favorable case, a satisfactory SNR of 30 dB was obtained.

3. Results

3.1. Bone phantom cylinder properties

Pulse-echo measurements were conducted to establish the reference values that will be used in the inversion process. As explained in Section 2.3.1, the geometric cross-section of the cortical layer of both cylinders is not uniform along their length, with a variation of about 10%. Nonetheless, the cortical synthetic material is assumed to be isotropic and homogeneous throughout the phantoms. Reference values of the cortical layer for both the healthy phantom and the osteoporotic one are depicted in Table 2.

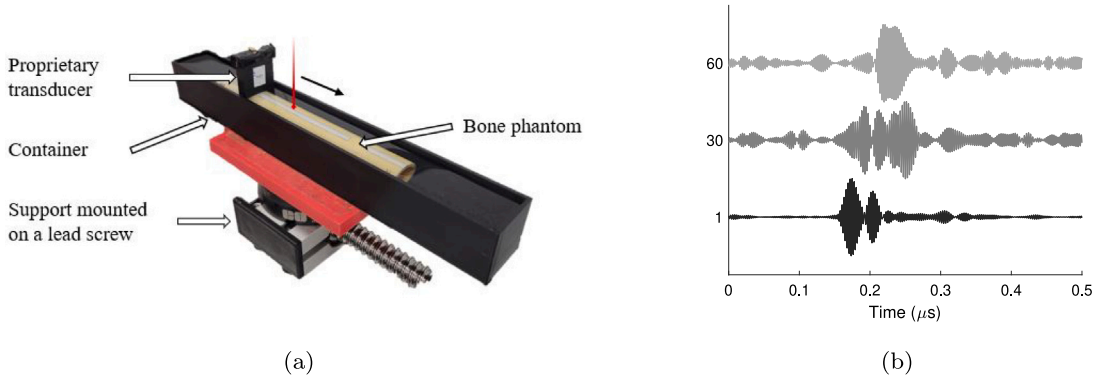

Fig. 3. (a) Experimental setup used for the axial transmission measurements with bone phantom cylinder immersed in fluid. (b) Representative signals for the immersed case at measurement points 1, 30 and 60.

Table 2
Reference property values for the healthy and osteoporotic bone phantom cylinders.

	Healthy bone phantom	Osteoporotic bone phantom
ρ (kg/m^3)	2295 ± 35	2085 ± 20
c_P (m/s)	2945 ± 65	2650 ± 35
c_S (m/s)	1730 ± 25	1535 ± 15
r^S (mm)	9.77 ± 0.50	9.96 ± 0.53
h^S (mm)	3.00 ± 0.23	2.97 ± 0.29

3.2. Parameters sensitivity

A study was conducted to evaluate how different parameters affect the dispersive trajectories of the ultrasonic guided wave modes. To this end, a variation of ±10% was applied to each parameter to assess its influence. The reference chosen parameters correspond to the central value of each parameter's range presented in Table 1. The variations were applied to c_P while keeping ν constant and equal to 0.24 (thus causing c_S to vary accordingly), as well as to r_S, h^S, and h^{fo}. The results are presented in Fig. 4. To observe the effect of each parameter on the dispersion curve trajectories, only mode points with an excitability value greater than −3 dB are retained.

Fig. 4 shows that variations of c_P, c_S and r_S globally influence the trajectories of dispersion curves, while h^S primarily affects low frequencies and h^{fo} impacts higher frequencies emphasizing the importance of using low frequency to minimize the impact of soft tissue layer. However, the variations presented in Fig. 4 are the result of modifying only one parameter at a time. Osteoporosis likely induce a simultaneous decrease of cortical thickness and wave velocities [24], further amplifying the differences between healthy and osteoporotic bone. This emphasizes the necessity of assessing all bone parameters simultaneously rather than each one independently.

3.3. Dispersion curves fitting

Experimental acquisitions were carried out with both phantoms under two conditions: with and without the outer fluid. Four measurements were taken for each case along the axis of the bone cylinders to extract experimental dispersion curves. The inversion procedure was then applied to both the healthy and osteoporotic phantoms in each scenario.

3.3.1. Dispersion curve fitting for free-field bone phantom cylinders

The experimental results shown in Fig. 5 are obtained by averaging the 2D-FFT plots for the corresponding four separate axial transmission measurements obtained for each cylinder. Averaging allows to consolidate spatial frequency information across multiple measurements to enhance clarity of the visual analysis. The semi-analytical points predictions are superimposed on the experimental dispersion curves with a −3 dB threshold applied to improve clarity. All values below −3 dB are automatically discarded to enhance visibility. As shown in Fig. 5, the alignment between experimental and simulated dispersion curves shows a good agreement for both phantoms, especially concerning the tangential slope of the curves, despite some differences that will be discussed in the next section.

3.3.2. Dispersion curve fitting for immersed bone phantom cylinders

In order to be closer to *in-vivo* conditions, the cylinders were immersed in a viscous fluid. The rationale is that the immersed setup provides a more accurate representation of real-world conditions. Olive oil was found to be a good candidate for this. In line with Mast's empirical study [34] and other relevant research [45], the suggested range for soft tissue density is between 900 kg/m^3 and 1200 kg/m^3. As mentioned in Section 2.2.1, olive oil was chosen thanks to its higher attenuation relative to water, while having similar sound speed and density to soft tissue. A layer of fluid was established atop the bone phantom cylinders, measuring 3 mm in thickness. The probe was positioned slightly below the fluid's surface, ensuring partial immersion. Results are presented similarly to Section 3.3.1. The semi-analytical point predictions are superimposed on the experimental dispersion curves with a −3 dB threshold. Fig. 6 corresponds to the best-fitting scenario for both cylinders. Due to the presence of olive oil surrounding the bone phantom cylinder, measurements were noisier in comparison with the free field scenario. Therefore, horizontal perturbations can be seen on the experimental dispersion curves for the immersed case.

3.4. Estimation of bone phantoms' properties

The average inverse characteristics for the four axial transmission measurements, optimized for each cylinder, are presented in Tables 3 and 4 for the free-field and immersed scenario, respectively, along with reference properties and their relative errors. Results demonstrate a close alignment of the mechanical property values, with errors below 3.0% for both scenarios. However, a larger discrepancy was obtained for the thickness and radius of the cortical shell for the free field case, which may be due to the fact that these parameters are inconsistent along the bone phantoms, and that their variations were averaged out during pulse-echo measurements.

In the free-field case, as shown in Fig. 5, the simulated dispersion curves align closely with the high-wavenumber modes across all frequencies. Consequently, the slope of the experimental curves is accurately captured, leading to precise predictions of the inverted properties such as wave velocities.

In contrast, for the immersed case in Fig. 6, the simulated dispersion curves align better at low frequencies with the low-wavenumber modes. This results in more accurate estimations of the geometrical parameters, emphasizing the critical role of low-frequency modes in determining bone geometry.

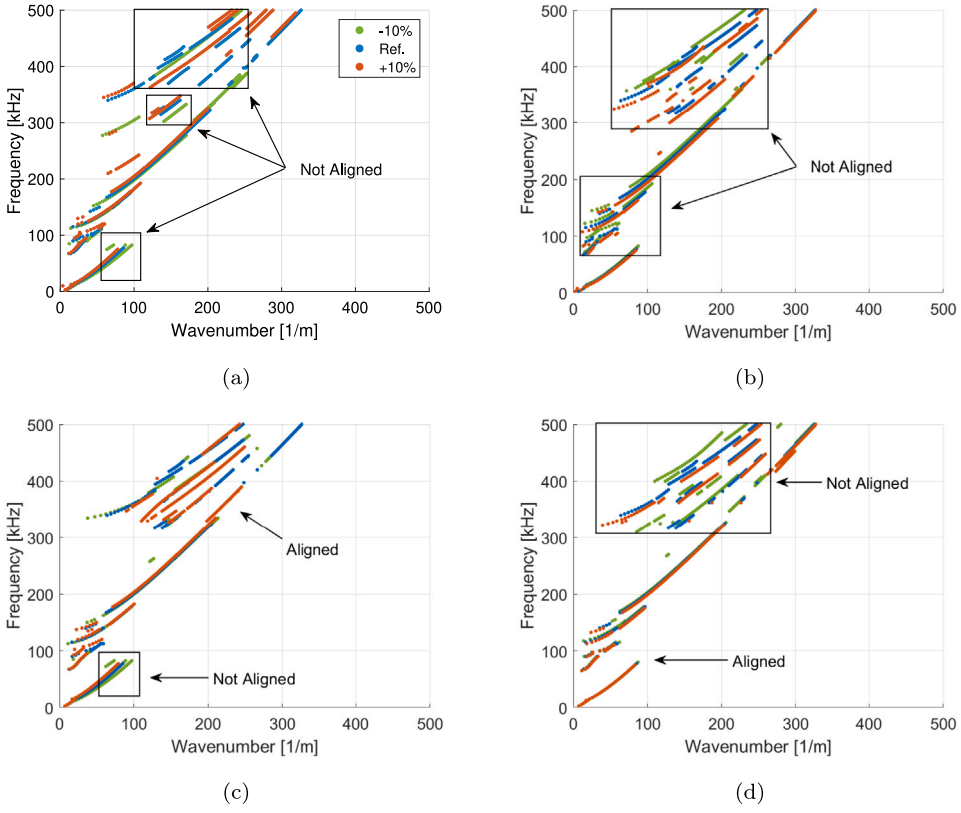

Fig. 4. Effect of parameter variations on ultrasonic guided waves dispersion curves. The blue lines represent the reference curves, the green lines correspond to the −10% variation, and the orange line to the +10% variation. Parameter influences are shown for: (a) c_P with ν held constant, (b) r^S, (c) h^S, and (d) h^{fo}. Arrows and rectangles highlight the key areas where changes take place.

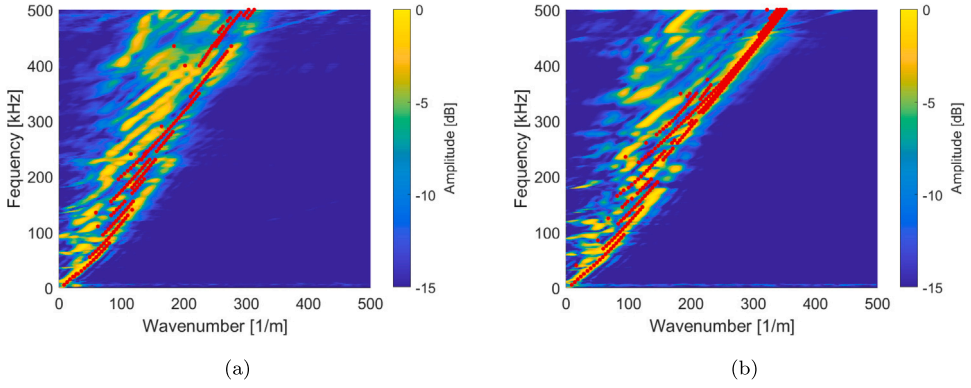

Fig. 5. Optimal fit between experimental and simulated dispersion curves for (a) healthy phantom, and (b) osteoporotic phantom. SAIGA-computed best fit are depicted by the red points atop experimental curves.

Table 3
Average inverse properties of phantom cylinders with their relative errors for the free-field scenario.

	Healthy cylinder			Osteo. cylinder		
	Ref.	Inv.	Err.%	Ref.	Inv.	Err.%
c_P (m/s)	2945 ± 65	2950 ± 141	0.17	2650 ± 35	2650 ± 115	0.00
c_S (m/s)	1730 ± 25	1725 ± 95	0.29	1535 ± 15	1550 ± 58	0.98
r^S (mm)	9.77 ± 0.50	10.13 ± 0.75	3.63	9.96 ± 0.53	9.25 ± 0.29	7.13
h^S (mm)	3.00 ± 0.23	2.90 ± 0.23	3.63	2.97 ± 0.29	3.3 ± 0.0	11.11

Table 4
Average inverse properties of phantom cylinders with their relative errors for the fluid-immersed scenario.

	Healthy cylinder			Osteo. cylinder		
	Ref.	Inv.	Err.%	Ref.	Inv.	Err.%
c_P (m/s)	2945 ± 65	3025 ± 95	2.72	2650 ± 35	2700 ± 100	1.89
c_S (m/s)	1730 ± 25	1750 ± 58	1.16	1535 ± 15	1575 ± 50	2.61
r^S (mm)	9.77 ± 0.50	9.75 ± 0.65	0.20	9.96 ± 0.53	9.75 ± 0.65	2.11
h^S (mm)	3.00 ± 0.23	2.90 ± 0.28	3.33	2.97 ± 0.29	3.1 ± 0.28	4.38

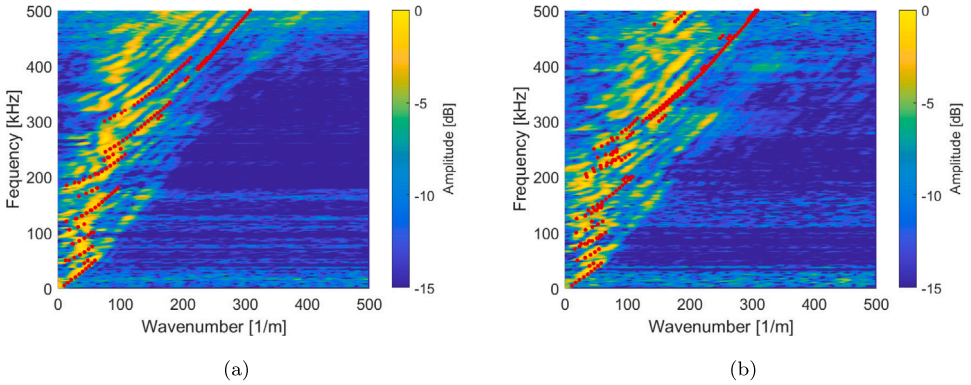

Fig. 6. Optimal fitting results between experimental and simulated dispersion curves for (a) healthy phantom cylinder, and (b) osteoporotic phantom cylinder immersed in olive oil. SAIGA-computed best fit are depicted by the red points atop experimental curves.

3.4.1. Estimated bulk-wave velocities

According to Tables 3 and 4, the average predicted values for longitudinal and shear wave velocities remain within the tolerance range of the reference values for both cylinders in all situations. In the free-field scenario, the error is found to be lower than 1%, while it slightly increases in the immersed scenario, albeit still remaining below 3%. This increase can be attributed to fluctuations in the surrounding fluid's thickness as well as its material properties due to changes in the experimental environment (change in oil temperature for example). Moreover, due to the presence of the outside fluid, experimental data are found to be much noisier, resulting in slight variation during the inversion.

3.4.2. Estimated radius and thickness

The estimated values of the thickness h^S and radius r^S fall within the baseline measurement margins of error. However, the relative errors are larger in the free-field case. The curvature of the bone phantom cylinders creates nearly point-like contact between the probe and the cortical shell, resulting in the generation of numerous circumferential modes. This complexity increases the challenge of fitting the dispersion curves accurately. In this specific case, the dispersion curves aligned more effectively with high-wavenumber modes, leading to more accurate velocity predictions but less precision in estimating the geometry. In contrast, when the cylinders are immersed in the fluid, this phenomenon is decreased as wave generation occurs over a broader area. Also, the dispersion curves aligned more effectively with low-wavenumber modes, which are strongly representative of the bone geometry.

Moreover, the osteoporotic cylinder has greater errors in radius and thickness measurements in both scenarios. This discrepancy may come from the overall geometry of the bone phantom as explained in Section 2.1.1. Additionally, reference values for cortical thickness in the osteoporotic model carry greater uncertainties. These subtle differences cumulatively result in larger percentage deviations during the inverse transformation.

3.4.3. Error propagation through the inversion process

The inversion process involves two main sources of uncertainty: grid discretization and experimental variability.

The grid resolution sets the precision of the parameter estimates. A finer grid improves accuracy but increases computational cost, while a larger grid step can introduce systematic errors. In this study, the parameter step sizes were chosen to balance these factors (see Section 2.2.2). For example, the step size for c_P is 100 m/s, leading to an uncertainty of ±50 m/s due to grid discretization which remain in the uncertainties range of the reference values, the same can be observed for other parameters. The relative errors for c_P and c_S (below 3%) confirm that the chosen resolution is appropriate.

We performed also four independent measurements on each cylinder. Each of the four axial transmission measurements was subject to experimental uncertainties, including noise, boundary inconsistencies, and slight variations in the bone phantom geometry. These uncertainties propagated through the cost function and affected the estimated parameters.

The reported standard deviations in Tables 3 and 4 for the inverted properties reflect the combined effects of these experimental uncertainties and grid resolution. For instance, the larger discrepancies observed for the radius (r^S) and cortical thickness (h^S) can be attributed to physical variations in the bone phantoms that are averaged out during the pulse-echo measurements. This averaging reduces the sensitivity of the inversion to localized inconsistencies but increases the relative error for these parameters compared to c_P and c_S.

3.4.4. Assessment of cortical layer density

Density is not directly assessed through the inversion process, but rather with a mathematical model [15,40]. As the model used in the simulation is isotropic, the resulting model parameters, which reflect the waveguide's stiffness, consist of two bulk wave velocities c_P and c_S, incorporating the mass density within the velocity parameters [16,46–48] and a stiffness ratio of elastic coefficients $C_{11}/C_{13} = 1 - 2(c_S/c_P)^2$. Using the reference values for density and bulk wave velocities, a linear interpolation can be made to express $C_{11} = \rho c_P^2$ and $C_{66} = \rho c_S^2$ as a function of density ρ [27]. As a consequence, c_P and c_S can also be expressed as a function of density as shown in Fig. 7.

Using inverse properties of both scenarios, density can be determined for the healthy and osteoporotic cylinder. As a result, for the free-field case, the results yield $\rho = 2300 \pm 10$ kg/m^3 and $\rho = 2096 \pm 12$ kg/m^3 for the healthy and osteoporotic cylinder respectively, leading to relative errors of 0.17% and 0.53%. For the immersed case, the density of healthy and osteoporotic cylinders are found to be respectively $\rho = 2343 \pm 28$ kg/m^3 and $\rho = 2120 \pm 5$ kg/m^3, with relative errors of 2.09% and 1.68%, which are quite acceptable at this stage.

4. Discussion

The cost function was computed across a multi-dimensional model grid, consistently identifying a global minimum for each acquisition. While navigating five or six dimensions is computationally demanding, SAIGA processes an immersed case in just over a minute but requires about eight days for all 9216 scenarios. However, since the dataset is generated once, subsequent inversions take only minutes. Using a parameter sweep over a finite set ensures a consistent global minimum, eliminating optimization concerns. Yet, predefined grid steps may introduce bias, though they were chosen to align with reference value uncertainties.

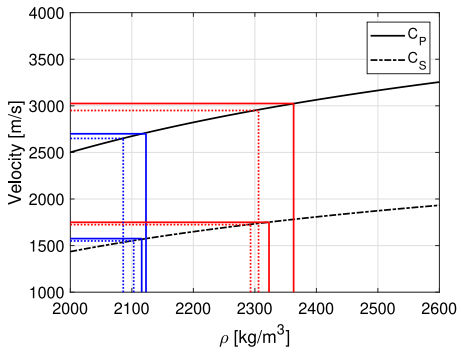

Fig. 7. Bulk velocities varying with the bulk density of the phantoms cortical material. (Blue lines) Inverse values for longitudinal and shear velocities of Osteoporotic phantom cylinder. (Red lines) Inverse values for longitudinal and shear velocities of Healthy phantom cylinder. Full lines depict the inverse values retrieved in the immersed scenario and the dot lines correspond to the free-field case scenario without outside fluid.

As mentioned in the previous study from our group [27], incorporating modal excitability into the cost function was crucial to improve the inversion procedure, significantly reducing the number of relevant modes. This reduction was achieved by weighting modes according to their excitability. By including only a limited number of modes, this approach minimizes data misfits during inversion. As demonstrated by Chaboty et al. [27], incorporating excitability into the inversion process reduces the percentage error by more than 10% compared to an inversion without this parameter. This methodology has proven effective in a 2.5D case scenario. Excitability ensures that all modes exhibiting high amplitudes are taken into account. Without incorporating excitability, the inversion process may be biased toward modes with high amplitudes over a broad frequency spectrum while neglecting lower-amplitude modes or those with high amplitudes over a narrow frequency range, which are particularly representative of geometry at low frequencies. This aspect is crucial as it allows for the inversion of the entire bone geometry rather than being limited to thickness estimation, as commonly observed in the literature where higher frequencies are employed. Furthermore, the relative errors obtained in our study remain within the same range as those reported by Bochud et al. and Minonzio et al. consistently below 5% [47,48].

Despite a favorable correlation between experimental and simulated results, especially at low frequencies (< 200 kHz) where curves aligned with great accuracy, there are discrepancies in the alignment of experimental and SAIGA-reconstructed dispersion curves at higher frequencies, as shown in Figs. 5 and 6. Several factors contribute to these differences.

Firstly, the accuracy of the SAIGA simulation-based approach hinges on the precision of the underlying model. Seyfaddini et al. [29] have demonstrated, through a comparison between SAIGA and the DISPERSE analytical model [49], that the number of degrees of freedom N_{dof} in the model is crucial for obtaining accurate results. While SAIGA remains significantly more efficient than the SAFE method, it still requires a sufficiently large value of N_{dof} to maintain precision. Unfortunately, increasing the accuracy and so the value of N_{dof} exponentially increases computation time. In the case presented in this manuscript, since the region of interest includes low frequencies, the number of patches of the model and the order of NURBS basis functions are considered acceptable, knowing that a single case takes around 70 s to compute. Doubling the number of elements would result in a simulation time of approximately 15 min. As a consequence, it would take around 96 days to process the 9216 cases required for this study, given our current computational capabilities. However, the inversion of the cortical bone phantom has yielded promising outcomes using the selected parameters, potentially indicating improved forecasts if the model's precision is enhanced.

Secondly, the complex geometry of cortical bone has been approximated by a cylindrical-like structure, making strong assumptions of symmetrical conditions. However, as shown in Fig. 1(b,c), the actual bone shape is not perfectly symmetric. Therefore, a difference in the simulated shape model and the real experimental geometry can explain such differences at higher frequencies. Nonetheless, estimated thickness and properties are found to be close to the reference ones, as shown in Tables 3 and 4.

The quality of experimental measurements is critical to the inversion process. The curvature of bone phantoms necessitates precise probe alignment with laser spots to extract dispersion curves accurately, as misalignment reduces amplitude and introduces variability. To mitigate this, multiple acquisitions were performed, though some variations persist. The cylindrical shape also supports circumferential modes, complicating inversion. However, since the method targets the radius, its asymmetry suppresses these modes, simplifying guided wave visualization (see Fig. 8). This suggests that the inversion process may be less sensitive to measurement fluctuations, particularly in *in-vivo* applications.

Finally, the properties of the cortical layer were defined as isotropic to match the phantoms used in this study. However, it is well known that cortical bones exhibit anisotropic or, at the very least, orthotropic behavior. To adapt the proposed method for *in vivo* bone characterization, the model should be further developed to account for the complexity of the medium. Future iterations could adopt approaches similar to those proposed by Pereira et al. [15,50], where the elastic coefficients vary with density based on a homogenization scheme developed by Vu et al. [40]. Alternatively, the model could include multiple layers within the cortical thickness to represent bone degradation from the endosteal to the periosteal region [11,17,20,51].

5. Conclusion

Using low frequencies in the context of axial transmission of ultrasonic guided waves demonstrated its ability to deduce the properties of bone cortex in an *in-vivo*-like configuration. The implementation of excitability requires fewer modes than other inversion techniques used at high frequencies. Using a combination of multiple high-excitability mode segments, the proposed SAIGA model achieved successful alignment with the amplitude of experimental dispersion curves. The study presented here builds on the work of Chaboty et al. [27], and offers a promising proof of concept for using the method in a clinical assessment of cortical bone properties. However, several limitations must be considered. The assumption of a simplified cylindrical bone model, while computationally efficient, does not fully capture the anatomical variability of real bones, particularly the radius. The current inversion scheme, although effective, remains computationally demanding, limiting the size of the dataset. Additionally, the experimental setup relies on precise alignment of the probe with laser measurements, which may introduce errors in practical *in vivo* conditions. A multi-element axial transmission probe must be developed to replace the use of laser measurements, as this technique is too sensitive for human body measurements.

The model will later evolve into a radius-shape bone, as presented in the discussion section. Improvements must be made to the SAIGA algorithm to reduce its computation time in order to increase the dataset with a smaller step for each parameter. The model will shift from an isotropic material to a transversely isotropic medium to better represent the bone cortex. Furthermore, the inversion scheme could be further improved using artificial intelligence (AI) techniques. This would increase its robustness, allowing it to evaluate bone properties based on the dispersion trajectories and amplitudes of guided wave modes within the waveguide.

The proposed method shows potential for clinical applications by providing a non-invasive tool to assess bone quality and detect early-stage osteoporosis. However, challenges such as patient variability

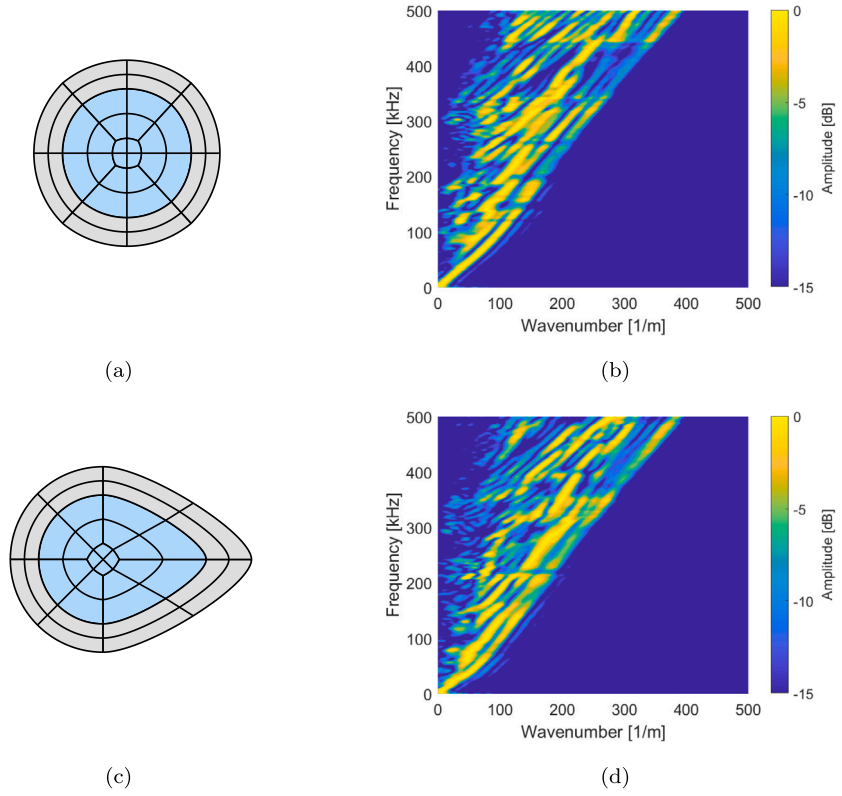

Fig. 8. Differences between a cylindrical geometry and a radius-like geometry. (a,c) Geometry of the two models. (b,d) Corresponding dispersion curves showing that fewer modes exist in the radius model.

and device reproducibility must be addressed. Differences in bone geometry, such as cortical thickness and outer diameter, require robust algorithms to ensure consistent results across diverse populations. Additionally, variability in device performance necessitates standardized protocols and self-calibrating mechanisms. Large-scale validation studies and the development of a comprehensive reference database would enhance the method's sensitivity and reliability. Collaborations with clinicians will be key to integrating this approach into clinical workflows, ensuring it aligns with practical diagnostic needs.

CRediT authorship contribution statement

Aubin Chaboty: Writing – review & editing, Writing – original draft, Validation, Software, Methodology, Investigation, Formal analysis, Conceptualization. **Vu-Hieu Nguyen:** Writing – review & editing, Supervision, Software, Methodology, Conceptualization. **Guillaume Haiat:** Writing – review & editing, Supervision, Resources, Conceptualization. **Pierre Bélanger:** Writing – review & editing, Supervision, Resources, Methodology, Funding acquisition, Conceptualization.

Declaration of Generative AI and AI-assisted technologies in the writing process

During the preparation of this work the authors used ChatGPT in order to improve English writing. This AI tool was not used for scientific analysis or data interpretation. After using this tool, the authors reviewed and edited the content as needed and take full responsibility for the content of the published article.

Declaration of competing interest

The authors declare that they have no known competing financial interests or personal relationships that could have appeared to influence the work reported in this paper.

Acknowledgments and funding

The authors would like to thank Nvidia for providing us with an Nvidia Quadro P6000 graphics card for our GPU simulations. This research was funded by Natural Sciences and Engineering Research Council of Canada: NSERC – RGPIN – 2020 – 05802. The authors acknowledge the support of the Laboratoire Franco-Canadien de Recherches Ultrasonores (LAFCUS).

Data availability

The data that support the findings of this study are available from the corresponding author upon reasonable request.

References

[1] World Health Organization, Assessment of Fracture Risk and Its Application to Screening for Postmenopausal Osteoporosis : Report of a WHO Study Group, World Health Organization, 1994.
[2] World Health Organization, Guidelines for Preclinical Evaluation and Clinical Trials in Osteoporosis, World Health Organization, 1998.
[3] P. Laugier, G. Haiat (Eds.), Bone Quantitative Ultrasound, Springer Netherlands, Dordrecht, 2011.
[4] A. de la santé publique du Canada, L'ostéoporose, 2014, Last Modified: 2024-02-15.
[5] P. Laugier, Q. Grimal (Eds.), Bone Quantitative Ultrasound: New Horizons, in: Advances in Experimental Medicine and Biology, Vol. 1364, Springer International Publishing, Cham, 2022.
[6] Q. Grimal, J. Grondin, S. Guérard, R. Barkmann, K. Engelke, C.-C. Glüer, P. Laugier, Quantitative ultrasound of cortical bone in the femoral neck predicts femur strength: results of a pilot study, J. Bone Miner. Res. Off. J. Am. Soc. Bone Miner. Res. 28 (2) (2013) 302–312.
[7] C.-C. Glüer, Quantitative ultrasound techniques for the assessment of osteoporosis: Expert agreement on current status, J. Bone Miner. Res. 12 (8) (1997) 1280–1288.

[8] D. Pereira, A. Le Duff, G. Painchaud-April, P. Belanger, Simulation-based inversion for the characterization of adhesively bonded joints using ultrasonic guided waves, IEEE Trans. Ultrason. Ferroelectr. Freq. Control 69 (7) (2022) 2400–2407.
[9] L. Bai, K. Xu, D. Li, D. Ta, L.H. Le, W. Wang, Fatigue evaluation of long cortical bone using ultrasonic guided waves, J. Biomech. 77 (2018) 83–90.
[10] A. Guha, M. Aynardi, P. Shokouhi, C.J. Lissenden, Identification of long-range ultrasonic guided wave characteristics in cortical bone by modelling, Ultrasonics 114 (2021) 106407.
[11] G. Haiat, S. Naili, Q. Grimal, M. Talmant, C. Desceliers, C. Soize, Influence of a gradient of material properties on ultrasonic wave propagation in cortical bone: Application to axial transmission, J. Acoust. Soc. Am. 125 (6) (2009) 4043–4052.
[12] M. Sasso, G. Haiat, M. Talmant, P. Laugier, S. Naili, Singular value decomposition-based wave extraction in axial transmission: application to cortical bone ultrasonic characterization, IEEE Trans. Ultrason. Ferroelectr. Freq. Control 55 (6) (2008) 1328–1332.
[13] K.M. Knapp, K.M. Knapp, G.M. Blake, T.D. Spector, I. Fogelman, Multisite quantitative ultrasound: Precision, age- and menopause-related changes, fracture discrimination, and T-score equivalence with dual-energy X-ray absorptiometry, Osteoporos Int. 12 (6) (2001) 456–464.
[14] D. Hans, L. Genton, S. Allaoua, C. Pichard, D.O. Slosman, Hip fracture discrimination study, J. Clin. Densitom. 6 (2) (2003) 163–172.
[15] D. Pereira, J. Fernandes, P. Belanger, Ex vivo assessment of cortical bone properties using low-frequency ultrasonic guided waves, IEEE Trans. Ultrason. Ferroelectr. Freq. Control 67 (5) (2020) 910–922.
[16] N. Bochud, Q. Vallet, Y. Bala, H. Follet, J.-G. Minonzio, P. Laugier, Genetic algorithms-based inversion of multimode guided waves for cortical bone characterization, Phys. Med. Biol. 61 (19) (2016) 6953–6974.
[17] G. Haiat, S. Naili, M. Ba Vu, C. Desceliers, C. Soize, Equivalent contributing depth investigated by a lateral wave with axial transmission in viscoelastic cortical bone, J. Acoust. Soc. Am. 129 (4) (2011) EL114–EL120.
[18] J. Foiret, J.-G. Minonzio, C. Chappard, M. Talmant, P. Laugier, Combined estimation of thickness and velocities using ultrasound guided waves: a pioneering study on in vitro cortical bone samples, IEEE Trans. Ultrason. Ferroelectr. Freq. Control 61 (9) (2014) 1478–1488.
[19] J.-G. Minonzio, J. Foiret, P. Moilanen, J. Pirhonen, Z. Zhao, M. Talmant, J. Timonen, P. Laugier, A free plate model can predict guided modes propagating in tubular bone-mimicking phantoms, J. Acoust. Soc. Am. 137 (1) (2015) EL98–EL104.
[20] S. Naili, M.-B. Vu, Q. Grimal, M. Talmant, C. Desceliers, C. Soize, G. Haïat, Influence of viscoelastic and viscous absorption on ultrasonic wave propagation in cortical bone: Application to axial transmission, J. Acoust. Soc. Am. 127 (4) (2010) 2622–2634.
[21] P. Moilanen, M. Talmant, V. Kilappa, P. Nicholson, S. Cheng, J. Timonen, P. Laugier, Modeling the impact of soft tissue on axial transmission measurements of ultrasonic guided waves in human radius, J. Acoust. Soc. Am. 124 (4) (2008) 2364–2373.
[22] T.N. Tran, L. Stieglitz, Y.J. Gu, L.H. Le, Analysis of ultrasonic waves propagating in a bone plate over a water half-space with and without overlying soft tissue, Ultrasound Med. Biol. 39 (12) (2013) 2422–2430.
[23] Y. Li, K. Xu, Y. Li, F. Xu, D. Ta, W. Wang, Deep learning analysis of ultrasonic guided waves for cortical bone characterization, IEEE Trans. Ultrason. Ferroelectr. Freq. Control 68 (4) (2021) 935–951.
[24] R.M. Zebaze, A. Ghasem-Zadeh, A. Bohte, S. Iuliano-Burns, M. Mirams, R.I. Price, E.J. Mackie, E. Seeman, Intracortical remodelling and porosity in the distal radius and post-mortem femurs of women: a cross-sectional study, Lancet 375 (9727) (2010) 1729–1736.
[25] P. Moilanen, Ultrasonic guided waves in bone, IEEE Trans. Ultrason. Ferroelectr. Freq. Control 55 (6) (2008) 1277–1286.
[26] D. Ta, W. Wang, Y. Wang, L.H. Le, Y. Zhou, Measurement of the dispersion and attenuation of cylindrical ultrasonic guided waves in long bone, Ultrasound Med. Biol. 35 (4) (2009) 641–652.
[27] A. Chaboty, V.-H. Nguyen, G. Haiat, P. Bélanger, Cortical bone plate properties assessment using inversion of axially transmitted low frequency ultrasonic guided waves, J. Acoust. Soc. Am. 156 (2) (2024) 954–967.
[28] F. Seyfaddini, H. Nguyen-Xuan, V.-H. Nguyen, Wave dispersion analysis of three-dimensional vibroacoustic waveguides with semi-analytical isogeometric method, Comput. Methods Appl. Mech. Engrg. 385 (2021) 114043.
[29] F. Seyfaddini, H. Nguyen-Xuan, V.-H. Nguyen, A semi-analytical isogeometric analysis for wave dispersion in functionally graded plates immersed in fluids, Acta Mech. 232 (1) (2021) 15–32.
[30] Z.A.B. Ahmad, J.M. Vivar-Perez, U. Gabbert, Semi-analytical finite element method for modeling of lamb wave propagation, CEAS Aeronaut. J. 4 (1) (2013) 21–33.
[31] J. Wu, F. Cubberley, Measurement of velocity and attenuation of shear waves in bovine compact bone using ultrasonic spectroscopy, Ultrasound Med. Biol. 23 (1) (1997) 129–134.
[32] M. Sasso, G. Haïat, Y. Yamato, S. Naili, M. Matsukawa, Dependence of ultrasonic attenuation on bone mass and microstructure in bovine cortical bone, J. Biomech. 41 (2) (2008) 347–355.
[33] D. Royer, E. Dieulesaint, Elastic Waves in Solids I: Free and Guided Propagation, Springer Science & Business Media, 1999, Google-Books-ID: SzwQ1UYspyQC.
[34] T.D. Mast, Empirical relationships between acoustic parameters in human soft tissues, Acoust. Res. Lett. Online 1 (2) (2000) 37–42.
[35] B. Alouache, D. Laux, A. Hamitouche, K. Bachari, T. Boutkedjirt, Ultrasonic characterization of edible oils using a generalized fractional model, Appl. Acoust. 131 (2018) 70–78.
[36] R. Chanamai, D.J. McClements, Ultrasonic attenuation of edible oils, J. Am. Oil Chemists Soc. 75 (10) (1998) 1447–1448.
[37] J. Yan, W.M. Wright, J.A. O'Mahony, Y. Roos, E. Cuijpers, S.M. Van Ruth, A sound approach: Exploring a rapid and non-destructive ultrasonic pulse echo system for vegetable oils characterization, Food Res. Int. 125 (2019) 108552.
[38] W. Karunasena, A.H. Shah, S.K. Datta, Wave propagation in a multilayered laminated cross-ply composite plate, J. Appl. Mech. 58 (4) (1991) 1028–1032.
[39] M.V. Predoi, M. Castaings, B. Hosten, C. Bacon, Wave propagation along transversely periodic structures, J. Acoust. Soc. Am. 121 (4) (2007) 1935–1944.
[40] M.-B. Vu, T. Nguyen-Sy, On the effective anisotropic elastic properties of porous hydroxyapatite, porous collagen, and cortical bone: A homogenization scheme with percolation threshold concept, Math. Mech. Solids 24 (4) (2019) 1091–1102, Publisher: SAGE Publications Ltd STM.
[41] M. Muller, D. Mitton, P. Moilanen, V. Bousson, M. Talmant, P. Laugier, Prediction of bone mechanical properties using QUS and pQCT: Study of the human distal radius, Med. Eng. Phys. 30 (6) (2008) 761–767.
[42] J.-Y. Rho, L. Kuhn-Spearing, P. Zioupos, Mechanical properties and the hierarchical structure of bone, Med. Eng. Phys. 20 (2) (1998) 92–102.
[43] V. Sansalone, S. Naili, V. Bousson, C. Bergot, F. Peyrin, J. Zarka, J.D. Laredo, G. Haiat, Determination of the heterogeneous anisotropic elastic properties of human femoral bone: From nanoscopic to organ scale, J. Biomech. 43 (10) (2010) 1857–1863.
[44] D. Alleyne, P. Cawley, A two-dimensional Fourier transform method for the measurement of propagating multimode signals, J. Acoust. Soc. Am. 89 (3) (1991) 1159–1168.
[45] M.O. Culjat, D. Goldenberg, P. Tewari, R.S. Singh, A review of tissue substitutes for ultrasound imaging, Ultrasound Med. Biol. 36 (6) (2010) 861–873.
[46] J.-G. Minonzio, M. Talmant, P. Laugier, Guided wave phase velocity measurement using multi-emitter and multi-receiver arrays in the axial transmission configuration, J. Acoust. Soc. Am. 127 (5) (2010) 2913–2919.
[47] N. Bochud, Q. Vallet, J.-G. Minonzio, P. Laugier, Predicting bone strength with ultrasonic guided waves, Sci. Rep. 7 (1) (2017) 43628.
[48] J.-G. Minonzio, N. Bochud, Q. Vallet, Y. Bala, D. Ramiandrisoa, H. Follet, D. Mitton, P. Laugier, Bone cortical thickness and porosity assessment using ultrasound guided waves: An ex vivo validation study, Bone 116 (2018) 111–119.
[49] B. Pavlakovic, M. Lowe, D. Alleyne, P. Cawley, Disperse: A general purpose program for creating dispersion curves, in: D.O. Thompson, D.E. Chimenti (Eds.), Review of Progress in Quantitative Nondestructive Evaluation, Springer US, Boston, MA, 1997, pp. 185–192.
[50] D. Pereira, G. Haiat, J. Fernandes, P. Belanger, Effect of intracortical bone properties on the phase velocity and cut-off frequency of low-frequency guided wave modes (20–85 kHz), J. Acoust. Soc. Am. 145 (1) (2019) 121–130.
[51] C. Desceliers, C. Soize, Q. Grimal, G. Haiat, S. Naili, A time-domain method to solve transient elastic wave propagation in a multilayer medium with a hybrid spectral-finite element space approximation, Wave Motion 45 (4) (2008) 383–399.